

## CO absorption in the Galactic Center cloud G0.253+0.015

1 ADAM GINSBURG,<sup>1</sup> ASHLEY T. BARNES,<sup>2</sup> CARA D. BATTERSBY,<sup>3</sup> ALYSSA BULATEK,<sup>1</sup> SAVANNAH GRAMZE,<sup>1</sup>  
2 JONATHAN D. HENSHAW,<sup>4,5</sup> DESMOND JEFF,<sup>1</sup> XING LU,<sup>6</sup> E. A. C. MILLS,<sup>7</sup> AND DANIEL L. WALKER<sup>8</sup>

3 <sup>1</sup>*Department of Astronomy, University of Florida, P.O. Box 112055, Gainesville, FL, USA*

4 <sup>2</sup>*European Southern Observatory (ESO), Karl-Schwarzschild-Straße 2, 85748 Garching, Germany*

5 <sup>3</sup>*University of Connecticut, Department of Physics, 196A Auditorium Road, Unit 3046, Storrs, CT 06269*

6 <sup>4</sup>*Astrophysics Research Institute, Liverpool John Moores University, 146 Brownlow Hill, Liverpool L3 5RF, UK*

7 <sup>5</sup>*Max-Planck-Institut für Astronomie, Königstuhl 17, D-69117 Heidelberg, Germany*

8 <sup>6</sup>*Shanghai Astronomical Observatory, Chinese Academy of Sciences, 80 Nandan Road, Shanghai 200030, P. R. China*

9 <sup>7</sup>*Department of Physics and Astronomy, University of Kansas, 1251 Wescoe Hall Dr., Lawrence, KS 66045, USA*

10 <sup>8</sup>*UK ALMA Regional Centre Node, Jodrell Bank Centre for Astrophysics, The University of Manchester, Manchester M13 9PL, UK*

11 (Dated: August 2023)

### ABSTRACT

13 We report JWST NIRCam observations of G0.253+0.015, the molecular cloud in the Central Molecular Zone  
14 known as “The Brick” with the F182M, F187N, F212N, F410M, F405N, and F466N filters. We catalog 59,266  
15 stars detected in all 6 filters using the `crowdsource` package. Stars within and behind The Brick exhibit  
16 prodigious absorption in the F466N filter that is produced by a combination of CO ice and gas. In support of this  
17 conclusion, and as a general resource, we present models of CO gas and ice and CO<sub>2</sub> ice in the F466N, F470N,  
18 and F410M filters. Both CO gas and ice may contribute to the observed stellar colors. We show, however, that  
19 CO gas does not absorb the Pf $\beta$  and Hu $\epsilon$  lines in F466N, but that these lines show excess absorption, indicating  
20 that CO ice is also present and contributes to observed F466N absorption. The most strongly absorbed stars  
21 in F466N are extinguished by  $\sim 2$  magnitudes, corresponding to  $> 80\%$  flux loss. This high observed absorption  
22 requires very high column densities of CO, requiring total CO column that is in tension with standard CO  
23 abundance and/or gas-to-dust ratios. There is therefore likely to be a higher CO/H<sub>2</sub> ratio ( $X_{CO} > 10^{-4}$ ) and  
24 more dust per H<sub>2</sub> molecule ( $> 0.01$ ) in the Galactic Center than the Galactic disk. Ice and/or gas absorption  
25 is observed even in the cloud outskirts, implying that additional caution is needed when interpreting stellar  
26 photometry in filters that overlap with ice bands throughout our Galactic Center. The widespread CO absorption  
27 in our Galactic Center hints that significant ice absorption is likely present in other galactic centers.

### 1. INTRODUCTION

29 G0.253+0.015, AKA “The Brick”, is among the best-  
30 studied infrared dark clouds in the Galaxy (Lis et al. 1991;  
31 Lis & Carlstrom 1994; Lis et al. 1994; Lis & Menten 1998;  
32 Lis et al. 2001; Longmore et al. 2012; Kauffmann et al. 2013;  
33 Rodríguez & Zapata 2013; Clark et al. 2013; Rathborne et al.  
34 2014a,b, 2015; Johnston et al. 2014; Bally et al. 2014; Pillai  
35 et al. 2015; Federrath et al. 2016; Marsh et al. 2016; Walker  
36 et al. 2016; Henshaw et al. 2019, 2022; Petkova et al. 2023).  
37 It is well-known for being dense and turbulent (Clark et al.  
38 2013; Rathborne et al. 2015; Federrath et al. 2016; Mills et al.  
39 2018; Henshaw et al. 2019, 2020) while exhibiting few signs  
40 of star formation, much less than is typical for such a mas-  
41 sive cloud (Longmore et al. 2012; Rodríguez & Zapata 2013;  
42 Mills et al. 2015; Walker et al. 2016, 2021). Several explana-  
43 tions have been offered for its relatively poor star formation:  
44 that it is young (Krijssen et al. 2015; Henshaw et al. 2016),

45 that it is highly turbulent (Federrath et al. 2016), that it is  
46 supported by magnetic fields (Pillai et al. 2015), and that it  
47 is many clouds along the line of sight (Henshaw et al. 2019,  
48 2022). Each of these explanations is likely to play some role  
49 in the cloud’s state and evolution.

50 Gas in the Galactic center is notably different from gas  
51 seen elsewhere in our Galaxy. It is richer in complex  
52 molecules (Jones et al. 2012) and warmer (Ao et al. 2013;  
53 Ginsburg et al. 2016; Krieger et al. 2017). Despite high gas  
54 temperatures, the dust in the CMZ is not terribly warm (Tang  
55 et al. 2021), so ice can accumulate on dust grains. Ice has  
56 long been seen in Galactic center mid-infrared spectra (Lutz  
57 et al. 1996; Chiar et al. 2000; Moneti et al. 2001), as has CO  
58 gas. Toward Sgr A\*, ice comprises a minority (< 10%) of  
59 the CO, which is dominated instead by gas, as expected given  
60 the high gas temperatures and extreme velocity dispersion of  
61 gas in the inner parsec (Moneti et al. 2001; Moultaka et al.

62 Beyond the inner parsec, though, the ice properties of  
 63 the Galactic center are little explored. A handful of Infrared  
 64 Space Observatory (ISO) spectra were taken toward various  
 65 positions, revealing both CO<sub>2</sub> and CO ice features, but lit-  
 66 tle has been written about them. An et al. (2011) and Jang  
 67 et al. (2022) used Spitzer IRS spectra to show that CO<sub>2</sub> ice is  
 68 common toward massive young stellar objects (MYSOs) in  
 69 the GC, and the O<sub>2</sub> is present in both gas and ice phases.

70 We present first JWST observations in narrow-band filters  
 71 toward The Brick, highlighting the first striking result that  
 72 CO ice is widespread. In Section 3, we describe the data pro-  
 73 cessing and catalog creation. Section 4 describes the mea-  
 74 surements of both star colors (§4.1) and diffuse gas emis-  
 75 sion (§4.2), then describes models of both CO gas (§4.3) and  
 76 ice (§4.4) absorption that explain some of the observed col-  
 77 lorts. We briefly discuss these results in Section 5 and then  
 78 conclude in Section 6. All of the analysis tools, including  
 79 the notebooks used to make the figures in this document, are  
 80 made available through a github repository<sup>1</sup>.

## 2. OBSERVATIONS

81 Observations were taken on 2022-08-15 as part of JWST  
 82 program 2221 in visit 001. This program consists of two  
 83 observations focused on The Brick, with 6 coordinated paral-  
 84 lel observations performed toward Cloud C. We present only  
 85 The Brick NIRCam observations in this work; the MIRI ob-  
 86 servations of The Brick and NIRCam and MIRI observations  
 87 of Cloud C will be presented in future works. We obtained  
 88 images in 6 filters listed in Table 1. We observed in narrow-  
 89 band filters in order to measure the extended line emission  
 90 from hydrogen recombination lines (Pa $\alpha$ , Br $\alpha$ , Pf $\beta$ ) and to  
 91 search for outflows (H<sub>2</sub> in F212N) and hot CO emission  
 92 from disks (F466N). The GTO program 1182 has observed  
 93 approximately the same field in broad-band filters.

94 In the NIRCam data we present, each image is comprised  
 95 of 24 exposures taken in the 6-TIGHT FULLBOX mosaic  
 96 strategy<sup>2</sup>, with 6 independent positions and 4 subpixel dithers  
 97 per position. Frames were read out in BRIGHT-2 mode with  
 98 2 groups per integration for a total exposure time of 1031  
 99 seconds.<sup>3</sup>

## 3. DATA PROCESSING

100 We downloaded the data from the MAST archive using  
 101 astroquery (Ginsburg et al. 2019; Brasseur et al. 2020).  
 102 We reprocessed data starting from L2 products, i.e., the cal-

<sup>1</sup> <https://github.com/keflavich/brick-jwst-2221/>

<sup>2</sup> <https://jwst-docs.stsci.edu/jwst-near-infrared-camera/nircam-operations/nircam-dithers-and-mosaics/nircam-primary-dithers>

<sup>3</sup> <https://jwst-docs.stsci.edu/jwst-near-infrared-camera/nircam-instrumentation/nircam-detector-overview/nircam-detector-readout-patterns>.

103 files, which include 24 individual flux-calibrated frames for  
 104 each filter.

105 Our reduction code is provided on github<sup>4</sup>.

### 3.1. Frame matching astrometry

106 Images were processed with a slightly modified version of  
 107 the JWST pipeline. The tweakreg command was run on  
 108 long-wavelength NIRCam data using the VVV DR2 catalog  
 109 (Saito et al. 2012) as an astrometric reference instead of the  
 110 Gaia catalog (there were too few stars detected in common  
 111 Gaia and by JWST, and most were saturated). We then cre-  
 112 ated a reference catalog based on the F405N catalog, which  
 113 had fewer saturated bright stars than F410M and therefore  
 114 more good associations with the ground-based NIR data. In  
 115 the make\_reftable.py script, we cut the F405N catalog  
 116 based on crowdsource quality flags ( $qf > 0.95$ , spread  
 117  $< 0.25$ ,  $frac > 0.9$ ). This reference catalog was then used  
 118 as the input to tweakreg for the other filters. We found that  
 119 the tweakreg pipeline did not adequately correct the image  
 120 registration to the absolute coordinates we provided, so we  
 121 manually cross-match the catalogs and computed shifts using  
 122 the realign\_to\_catalog and merge\_a\_to\_b functions  
 123 in align\_to\_catalogs.py.

### 3.2. 1/f noise removal

124 The narrow-band filters, particularly F187N, F212N, and  
 125 F466N, exhibited significant ‘streaking’ noise that is strongly  
 126 evident in the low-signal regions of the image, i.e., the ma-  
 127 jority of the molecular cloud. This streaking is caused by 1/f  
 128 noise in the detectors (STScI helpdesk ticket INC0181624).  
 129 As a first pre-processing step, we performed ‘destreaking’  
 130 on each detector following a method suggested by Massimo  
 131 Roberto (priv. comm.), in which:

- 132 1. Each detector is split into four horizontal quadrants  
 133 with width 512 pixels and height 2048 pixels.
- 134 2. The median across the horizontal axis is calculated, re-  
 135 sulting in a 2048-pixel array.
- 136 3. In a slight departure from Massimo’s method, we  
 137 then smooth the median-array using a 1D me-  
 138 dian filter with length that varies depending on  
 139 the filter. ‘F410M’: 15, ‘F405N’: 256,  
 140 ‘F466N’: 55, ‘F182M’: 512, ‘F187N’:  
 141 256, ‘F212N’: 512. We found that the orig-  
 142 inal method, which was to obtain a single constant at  
 143 this step, turned the destreaking process into a high-  
 144 pass filter and therefore removed significant extended  
 145 emission.

<sup>4</sup> <https://github.com/keflavich/brick-jwst-2221>

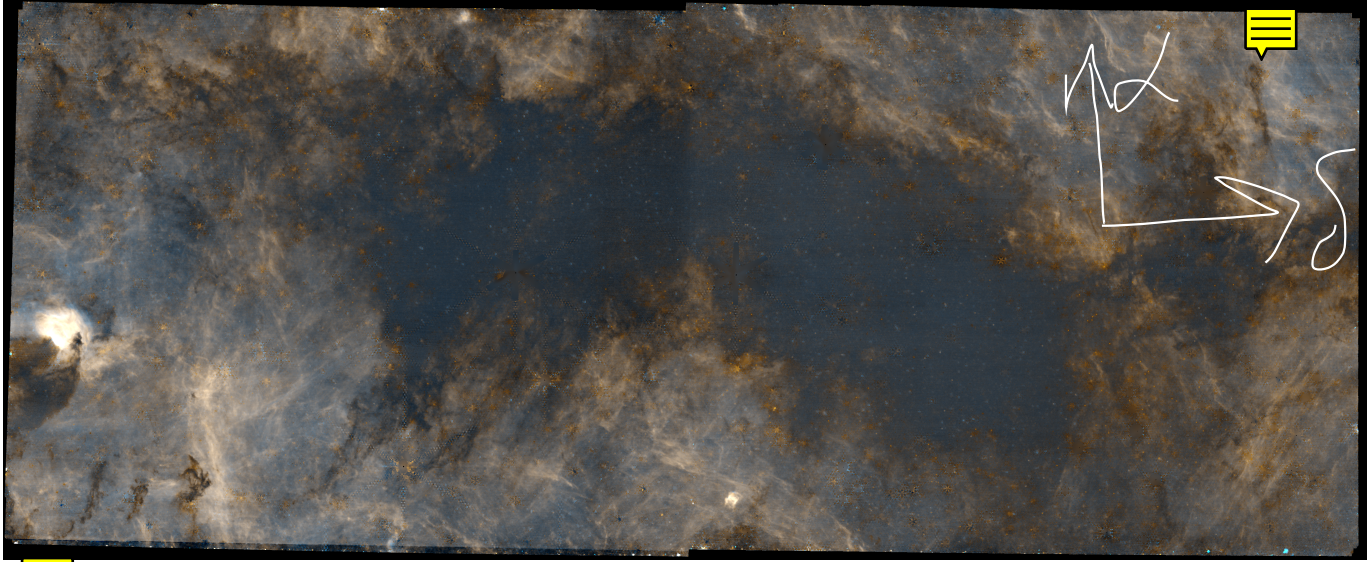


**Figure 1.** The full-field star-subtracted image as described in §3.5. This image captures extended recombination line emission from  $\text{Pf}\beta$  and  $\text{Hue}$  in F466N (466m410, continuum-subtracted F466N, is shown in blue-green) and  $\text{Br}\alpha$  in F405N (405m410, continuum-subtracted F405N, is shown in yellow), highlighting The Brick as the dark cloud spanning the image. Most of the image looks like shades of brown with a tinge of blue, though, which is because both the F466N and F405N filters contain recombination lines ( $\text{Pf}\beta + \text{Hue}$  and  $\text{Br}\alpha$ , respectively). The color is therefore bluer when dust extinction is the dominant absorption effect and browner when CO absorption is dominant (see §4.2). Note that significant artistic license has been taken to fill in regions where star PSFs have made pixel fluxes unrecoverable; the image represents the overall structure of the cloud well, but many small-scale features are artifacts of the star subtraction. Declination is on the X-axis, contrary to convention. A full resolution version is available online (which we hope to make available through the journal). Figure 3 shows the same figure with coordinates labeled.

150     4. We subtract the median array from each quadrant, then  
151     add back the smoothed median.

152     We evaluated the effectiveness of this process by eye.  
153     While the original destreaker completely removed the 1/  
154     horizontal features, it also removed all of the extended back-  
155     ground. The modified version removed most of the horizon-  
156     tal features while preserving the large-scale extended struc-  
157     ture. It is likely that some intermediate-scale features (i.e.,  
158     physical features comparable to 512 pixels across) are not re-  
159     covered by this procedure, which will need to be accounted  
160     for in analysis of the extended emission.

161     3.3. Photometric and Astrometric Cataloging  
162     For photometry of unsaturated stars, we use the  
163     crowdsourcing python package (Schlafly 2021). We used  
164     a PSF model from `webbpsf`. Because we were using mo-  
165     saiced images, the `webbpsf` PSF is not a perfect represen-  
166     tation of the data; each individual frame had to be shifted  
167     and drizzled to form our final images. We therefore used the  
168     `webbpsf` model smoothed by a small amount, 0.05 pixels,  
169     as our PSF. We experimented with other PSFs and found that  
170     this approach was good enough, but it is not quantitatively  
171     optimal. Furthermore, for the short wavelength bands, we  
172     adopted the PSF for a single detector (NRCA1 or NRCB1 as  
173     appropriate) for the full frame, since `webbpsf` does not pro-  
174     vide a tool to produce a PSF grid across the whole module.

175     We then replace the flux measurements obtained for sat-  
176     urated stars with those from the saturated star catalog. If a  
177     star was unsaturated in one filter but saturated in others, we  
178     replace the flux in the saturated filter if the positions in the  
179     compared catalogs agree to within 0.05" (0.1") in the short  
180     (long) filters. We also replace the position with the fitted po-  
181     sition of the saturated star. When there is no match within  
182     the threshold radius, we add the saturated star to the catalog.  
183     These entries in the catalog have different information since  
184     they were not extracted by `crowdsourcing`, and they are de-  
185     noted in the catalog with the `replaced_saturated` flag.

### 186     3.4. Catalog matching

187     We assemble a catalog consisting of all sources found in  
188     any of our six filters. To assemble the coordinate list, we start  
189     with all coordinates in the F405N catalog, then for each other  
190     filter, we add all sources that do not have a match in the exist-  
191     ing catalog within  $d < 0.15''$ . The cross-matched catalog shows a large  
192     peak for matches within  $d < 0.1''$  with large tails at greater  
193     separation. The resulting crossmatched catalogs had stan-  
194     dard deviation positional offsets  $< 0.02''$  (Table 1), with the  
195     smallest for F410M, likely because of the similarity in wave-  
196     length to the reference filter F405N. The order-of-magnitude  
197     smaller offset noise seen for F410M than the other filters sug-  
198     gests that the large scatter is driven by changes in the PSF  
199     with wavelength. We do not concern ourselves further with  
200     astrometry in this manuscript, but caution that our catalogs

**Table 1.** Observations

Filter Name	RMS Offset "	90th percentile mag(AB)	# of sources
F182M	0.019	20.4	337914
F187N	0.020	20.3	213521
F212N	0.019	19.5	235454
F405N	-	19.5	91860
F410M	0.003	19.6	95746
F466N	0.019	19.6	80883

The RMS offset reports the standard deviation of the source position difference between the specified filter and the reference filter, F405N. The 90th percentile column reports the 90th percentile magnitude in the catalog to give a general sense of depth.

likely are not yet of sufficient quality to support proper motion measurements.

For subsequent analysis, we then select all sources with magnitude errors  $\sigma_m > 0.1$ , ‘quality factor’  $qf \leq 0.6$ ,  $spread > 0.25$ , or  $fracflux < 0.8$ . These choices select for round, pointlike, unblended stars.

We find 377,593 stars with a good measurement in at least one filter, and 59,266 with good measurements in all 6 filters. The number found in each filter is given in Table 1.

### 3.5. Starless Image Creation

For comparison of star locations to extinction features, we prefer to work with an image with stars removed. A starless image is the natural residual of an image that has been processed through a PSF photometry routine that appropriately accounts for the non-point-source background.

ever, such images tend to have substantial residual features. To create a cleaner starless image, we take the difference between the narrow-band and medium-band images after appropriately scaling the narrow-band image. The F405N image is convolved with a 0.3 pixel Gaussian to better match the PSF of the F410M filter. We then scale F405 by 0.1782,

which is a factor empirically determined to best match star

PSF peaks; the theoretical ratio of filter bandwidths is 0.103.

We produce a line-free F410M image, labeled 410m405

by subtracting the scaled F405N image from the F410M.

We produce a star-free F405N image, labeled 405m410, by

subtracting the (theoretically continuum-only) 410m405 im-

age. We then produce a somewhat star-free F466N image,

which we label 466m410, by subtracting the 410m405 im-

age scaled by 0.8; this image has much greater residuals,

since the wavelengths do not overlap and differences in dust

extinction (and ice absorption; see below) render the sub-

traction somewhat poor. Nevertheless, the stars are largely

removed, and in particular, their extended PSFs are miti-

gated. The subtraction process is recorded in the notebooks

BrA\_separation\_nrca.ipynb, BrA\_separation\_nrcb.ipynb,

F466N\_separation\_nrca.ipynb, and F466N\_separation\_nrcb.ipynb.

This process still left significant residuals throughout both the 405m410 and 466m410 images. To further remove stars - at this stage, purely for aesthetic purposes - we identify the locations of significant residuals and mask them out, then interpolate across them. We perform this process iteratively, using larger masks for stars with more extended PSF features and smaller masks for more compact, fainter stars. The details of the process were largely decided ‘by hand’, i.e., testing a small variation in a parameter (e.g., the mask size) and revising if it did not look good. We also created custom masks to remove residuals from extended PSFs. The masking process is recorded in the StarDestroyer\_nrca.ipynb and StarDestroyer\_nrcb.ipynb notebooks. After each module was fully star-subtracted, the images were merged in the Stich\_A\_to\_B.ipynb notebook.

Figure 1 shows the merged full-frame image.<sup>5</sup> For comparison, Figure 2 shows the Spitzer GLIMPSE (Churchwell et al. 2009) image of The Brick, which helped establish the cloud as an iconic dark cloud; the level of detail, and density of stars, revealed by the JWST observations opens a new window into our Galaxy’s most extreme infrared dark cloud. Figure 3B shows the raw image before removing the stars, and Figure 3A shows the version with stars removed.

## 4. RESULTS

The Brick stands out in infrared images as a dark feature against a background both of stars and of diffuse emission (e.g., Figures 1 and 2). We start by highlighting that The Brick is an extinction feature, but that it exhibits peculiar colors in the F466N filter in §4.1. We then discuss the diffuse emission from recombination lines in §4.2. Both from absorption of this diffuse emission and from the colors of extincted stars, we infer that gas (§4.3) and ice (§4.4) is contributing to the line-of-sight absorption that defines The Brick.

### 4.1. Some stars are too blue in F466N colors

The first intriguing result from these data is that, in colors including F466N, which is our longest-wavelength filter, the stars that are most extinguished appear too blue. In general, dust extinction causes reddening, i.e., the shorter-wavelength photons are more attenuated than the long-wavelength photons; in this case we see the inverse effect happening, so we refer to it as bluing. This feature is evident in color-magnitude and color-color diagrams (Figure 4). Figure 4 shows a color-CCD

<sup>5</sup> [https://www.dropbox.com/scl/fi/7h15r44vcja9a3yle8wlw/BrickJWST\\_merged\\_longwave\\_narrowband\\_rotated\\_lighter.png?rlkey=zgr7oas6vk2oh1ryzu6u8404r&dl=0](https://www.dropbox.com/scl/fi/7h15r44vcja9a3yle8wlw/BrickJWST_merged_longwave_narrowband_rotated_lighter.png?rlkey=zgr7oas6vk2oh1ryzu6u8404r&dl=0)

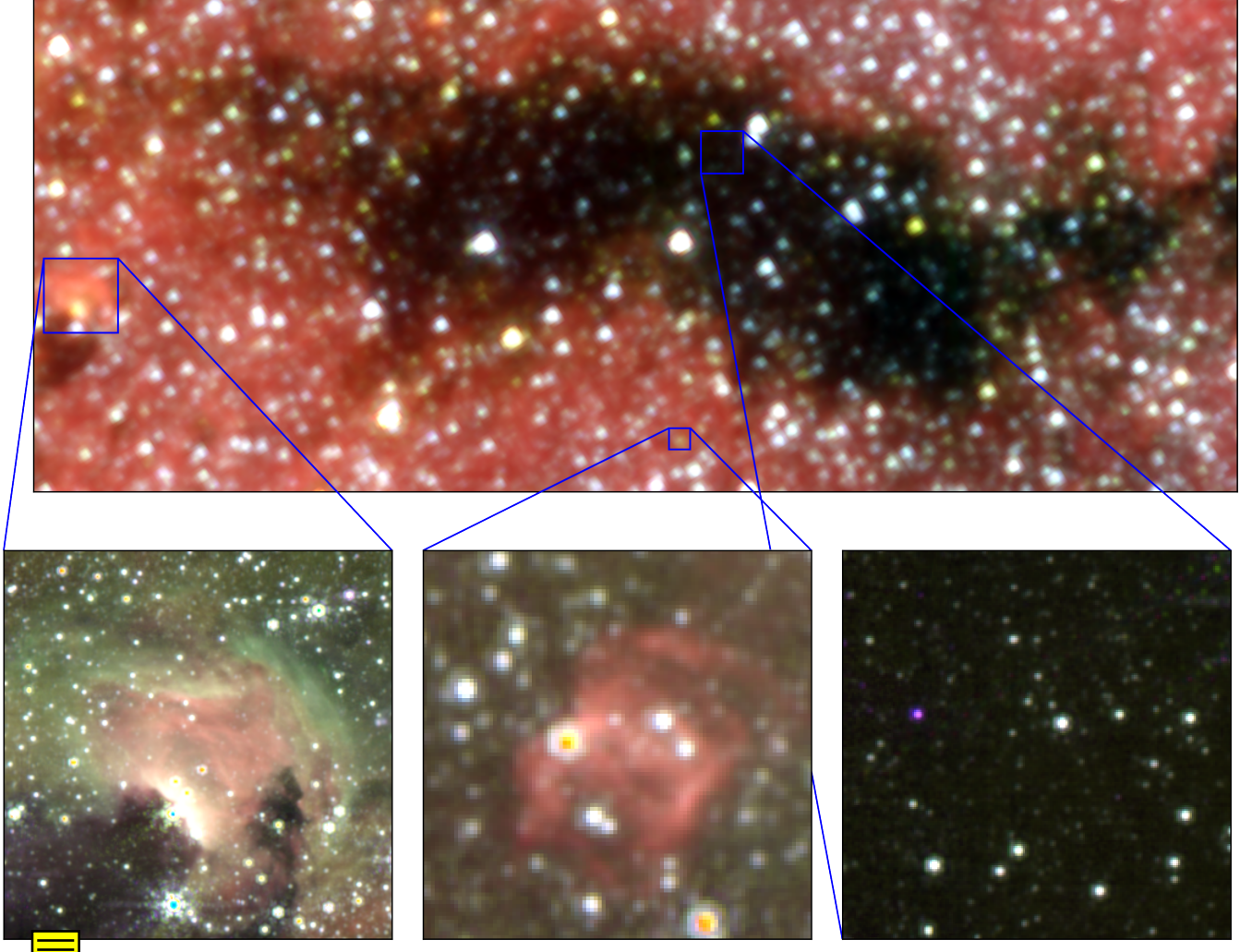


**Figure 2.** Three-color Spitzer image (red is  $5.6 \mu\text{m}$ , green is  $4.5 \mu\text{m}$ , blue is  $3.6 \mu\text{m}$ ) with insets showing JWST data (red is F405N, green is F466N, blue is F410M). The insets highlight the HII region G000.208-00.003 (left), the source [RZ2013] JVLA 1, which is also [IMS2012] B (middle), and the center of the water maser source field (right). In the right inset, there is a purple source toward center-left, which is one of the F466N ‘dropouts’, i.e., a highly blued source with CO absorption. Note that declination is on the X-axis, contrary to convention.

284 color color diagram with an extinction vector from Chiar &  
 285 Tielens (2006, hereafter CT06) overlaid demonstrating that  
 286 the F466N color goes the wrong direction. We see excess ab-  
 287 sorption in the F466N filter of roughly 0.035 magnitudes per  
 288  $A_V$  with substantial scatter.

289 The blue stars in F410M/F466N are seen at the edge  
 290 of the cloud. Figure 3 shows the location of these bluest  
 291 ( $[\text{F}466\text{N}] - [\text{F}410\text{M}] < -0.1$ ) stars. The most extinguished stars,  
 292 which are the reddest in most colors but are blue in  
 293 involving F466N, primarily seen along the outskirts of  
 294 the cloud. Figure 4 shows stars color-coded by  $[\text{F}187\text{N}] -$   
 295  $[\text{F}405\text{N}]$  color. The interior of the cloud appears relatively  
 296 blue in Fig. 4a because only low-extinction stars were detected  
 297 in the shorter-wavelength F187N filter. Figure 4b highlights  
 298 that colors not involving the F466N filter are consistent with  
 299 extinction.

#### 300 4.2. The F466N recombination lines also tend to blue

301 The diffuse emission circumscribing The Brick, seen in  
 302 F405N and F466N in Figure 1, is comprised primarily of  
 303  $\text{Br}\alpha$  (F405N) and  $\text{Pf}\beta$  plus  $\text{H}\epsilon$  (F466N) emission. Figure ~~~~~~  
 304 5 shows where these lines reside with respect to the trans-  
 305 mission profiles of the filters. There are no other expected  
 306 sources of emission in this band, as there are no known PAH  
 307 features in the  $4-5\mu\text{m}$  range and free-free emissio~~~~~  
 308 expected to be weaker by  $\sim 100\times$  in the narrow bands.

309 The ratio of hydrogen recombination lines is governed by  
 310 simple rules under the assumption of Case B recombination,  
 311 which is expected at moderate densities. The expected ra-  
 312 tio of  $\text{Pf}\beta / \text{Br}\alpha$  under Case B recombination at electron  
 313 temperature  $T_e \sim 5000 - 10^4 \text{ K}$  is  $R_{\text{Pf}\beta/\text{Br}\alpha} = 0.202$   
 314 (Storey & Hummer 1995). The ratio of  $\text{Pf}\beta + \text{H}\epsilon$ , the sum  
 315 of the two lines in F466N, to  $\text{Br}\alpha$  is  $R_{(\text{Pf}\beta + \text{H}\epsilon)/\text{Br}\alpha} =$

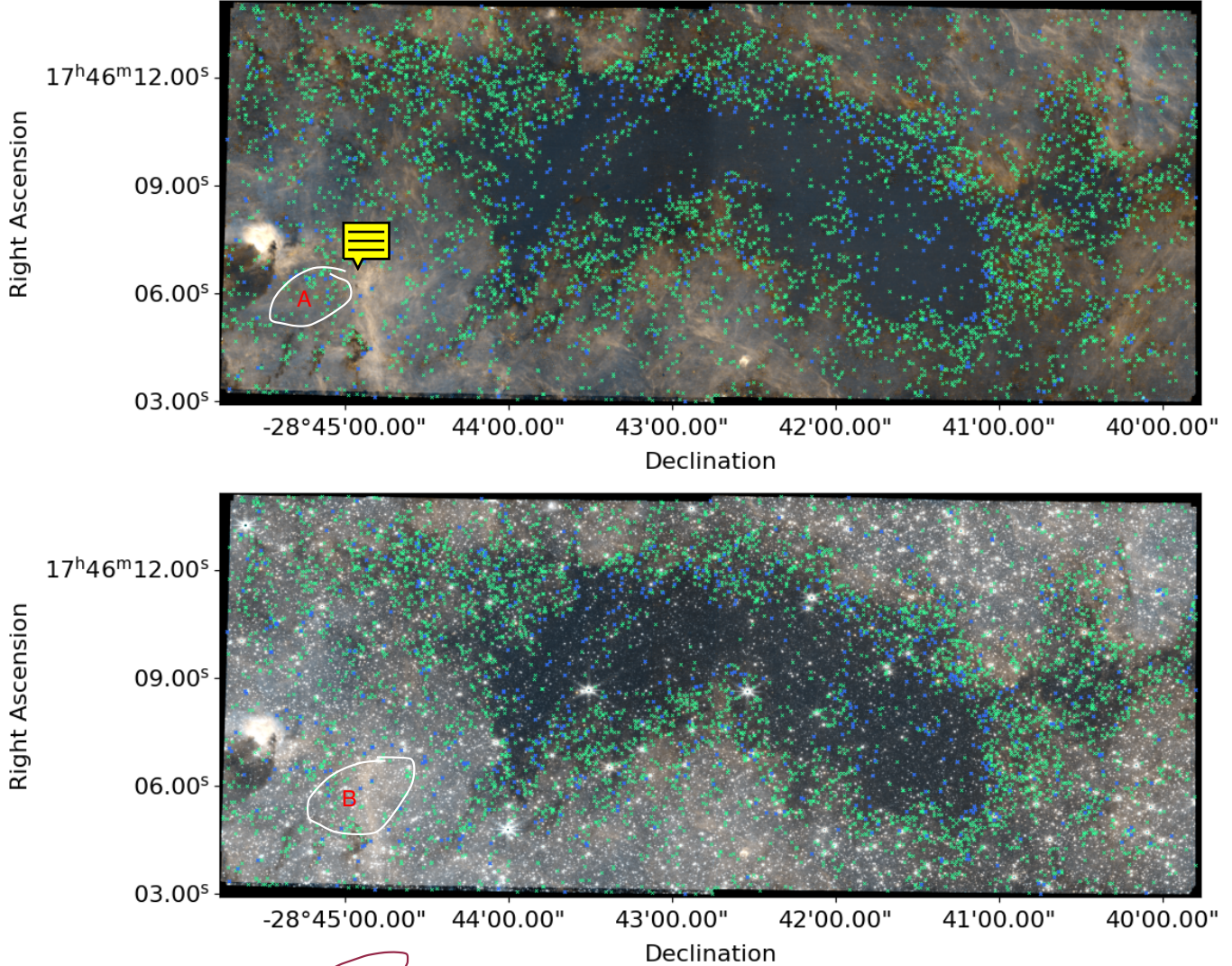


**Figure 3.** Stars with blue F466N/F410M colors ( $[F466N]-[F410M] < -0.75$  in green and  $< -1.75$  in blue) shown with X's on the star-subtracted RGB (top) and not-subtracted (bottom) image. Note that declination is on the X-axis, contrary to convention.

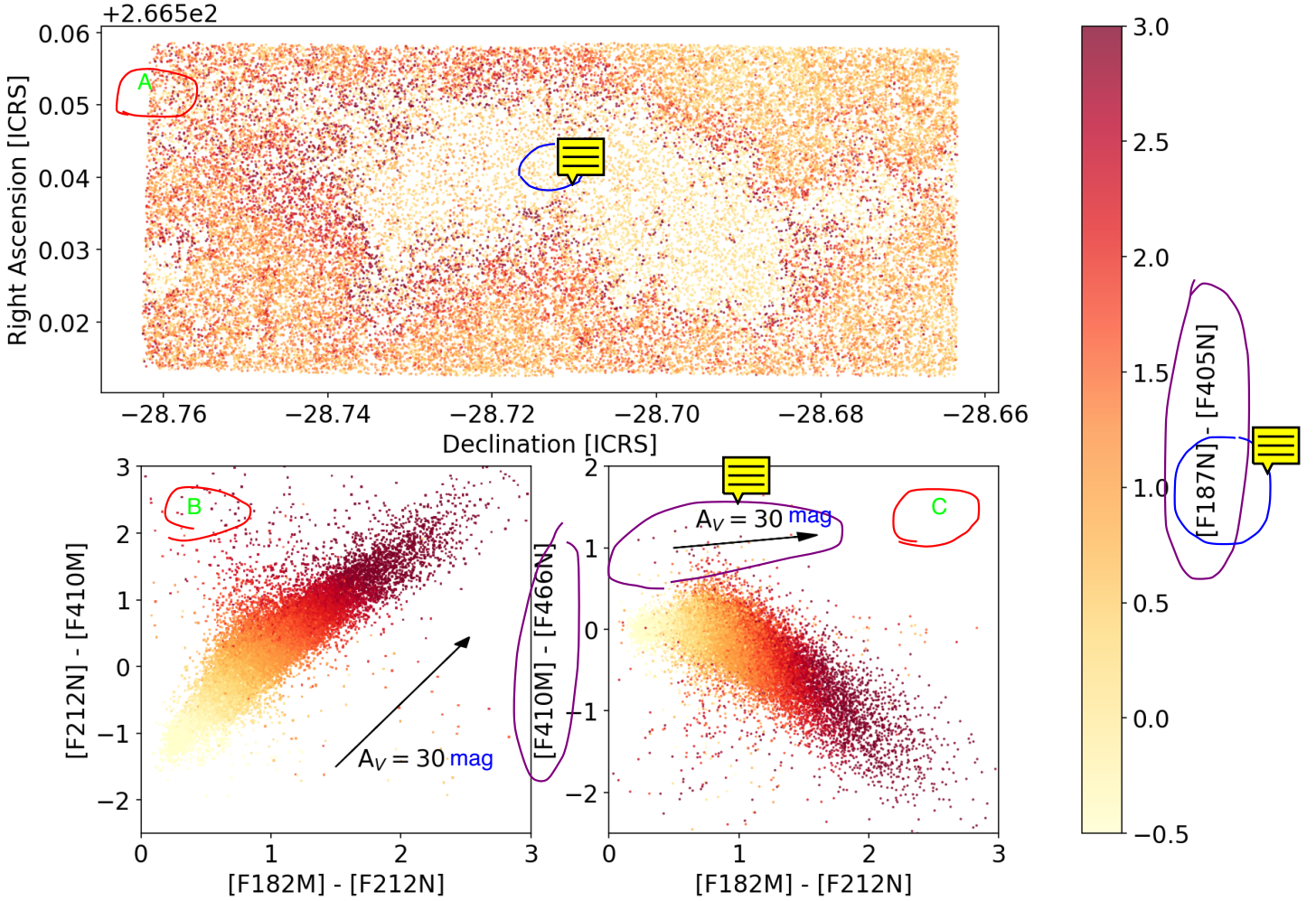
0.234. For  $A_V = 30$ , the average foreground extinction toward the CMZ (Launhardt et al. 2002; Nogueras-Lara et al. 2021), using a CT06 extinction curve, this rises to  $R_{(Pf\beta+Hue)/Br\alpha}(A_V = 30) = 0.269$ . At higher extinction, this ratio (F466N/F405N) is expected to rise. However, contrary to this expectation, we see the F466N/F405N ratio decreasing along the edge of The Brick (Figure 3). In these color figures, bluer regions have higher F466N/F405N, while browner regions have lower. In general, the edges of the dark cloud are brown. We are therefore seeing that, in higher extinction regions, the ratio is the inverse of what is expected from dust extinction.

#### 4.2.1. CO absorption of the F466N recombination lines

There are additional absorption processes that affect only the F466N filter. The F466N filter covers both CO gas and ice features (we will discuss these further in §4.3 & §4.4),

and therefore we expect the ratio F466N/F405N to be lesser, not greater, than the theoretical Case B recombination value if CO ice is present along the line of sight. We observe this decrease: the edges of the molecular cloud appear brown in Figure 1, indicating a relative deficiency in the F466N filter compared to regions further from the molecular cloud.

To assess whether the absorption is caused by CO or ice, we model the absorption caused by CO. Figure 5b shows a CO line profile modeled assuming local thermodynamic equilibrium (LTE) conditions for a column density of  $N(\text{CO})=5\times 10^{16} \text{ cm}^{-2}$ , temperature  $T = 50 \text{ K}$ , and linewidth  $\sigma = 5 \text{ km s}^{-1}$ . This figure shows that there is a 100 km s<sup>-1</sup> offset between the CO gas lines and the hydrogen recombination lines. The broadest linewidths observed in the molecular gas are  $\sim 20 \text{ km s}^{-1}$  (Henshaw et al. 2019), so CO lines are unlikely to strongly absorb the recombination line emission.



**A panel:** Location of the 33798 stars with detections in all 6 bands that met the quality criteria specified in §3.3 and that have  $[F410M] < 18.5$ . Note that declination is on the X-axis. **B panel:** Comparison of  $F182M$ - $F212N$  to  $F212N$ - $F410M$  color. **C panel:** Comparison of  $F182M$ - $F212N$  to  $F466N$ - $F410M$  color. An extinction vector  $A_V = 30$  mag along the CT06 curve is shown, corresponding to about 1 magnitude of  $[F182M]$ - $[F212N]$  color excess. In the bottom-left panel, the extinction vector retains the shape of the CCD assuming all stars have roughly zero color, while in the right panel, it does not; instead, there is significant bluing of  $[F410M]$ - $[F466N]$  color with increasing extinction. The correlation between the colorbar and each of the bottom-left panel colors indicates that all of these colors align with dust extinction. We adopted a sequential colormap to emphasize the most extincted sources, which show up as dark red...in all panels.

By contrast, CO ice produces broadband absorption that affects both the  $Pf\beta$  and Hue lines. Figure 5 shows CO and  $CO_2$  absorption profiles both with assumed  $N(CO) = 10^{17} \text{ cm}^{-2}$ . The CO ice profile overlaps significantly with both the recombination lines in the F466N filter. CO<sub>2</sub> ice, shown in panel M, significantly affects the F410M filter but has little effect on the Br $\alpha$  line. Based on this figure, the observation that there is excess absorption of the diffuse F466N, we conclude that CO ice, and not CO gas, is absorbing Pfund  $\beta$  and Humphreys  $\epsilon$  emission.

#### 4.3. CO Gas

As shown in Figure 5, the  $^{12}\text{CO}$  lines in the F466N band can produce significant absorption against stellar continuum light. In this section, we evaluate whether CO gas can pro-

duce the observed stellar colors. We already saw in §4.2 that CO gas is unlikely to produce selective extinction of  $Pf\beta + \text{Hue}$ . We find here that CO gas contributes to, but does not dominate, the total absorption in F466N.

We model this absorption as a function of temperature, column density, and linewidth assuming local thermodynamic equilibrium (LTE) conditions. Details of this modeling is given in an associated Jupyter notebook, COFundamentalModeling.ipynb, that can be found in the associated github repository. The model implementation is in the pyspeckit-models package, which implements models compatible with pyspeckit (Ginsburg et al. 2022). We used transition and level tables from the exomol database (Tennyson et al. 2016) derived from Li et al. (2015)

What is the CO optical depth and does  $^{13}\text{CO}$  need to be taken into account?

Mixing emission and absorption lines will confuse. Better to use the Figure form shown in Appendix B.

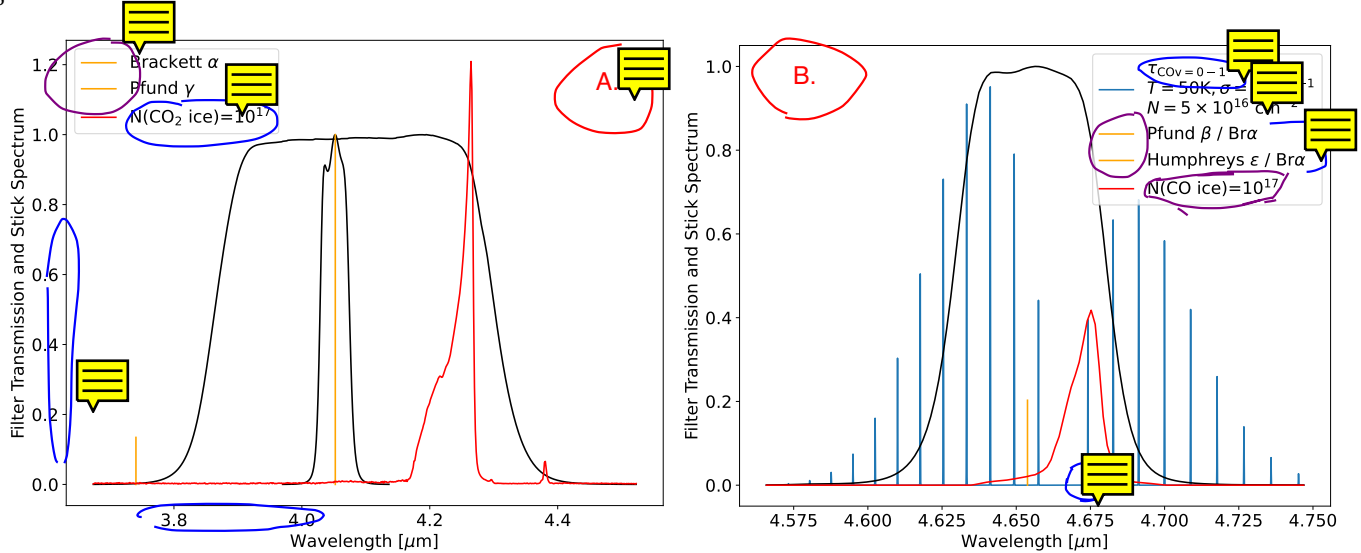


**Figure 5.** Transmission curves and stick spectra of hydrogen recombination emission lines and CO gas absorption lines in the NIRCam long-wavelength filters analyzed here. F410M and F405N are shown on the left and F466N is shown on the right. This is a schematic figure showing where lines and ice features appear and what their relative strengths are, but the amplitude scales are arbitrary. The CO gas, discussed in §4.3, overlaps extensively with the F466N filter. Both the F466N and F405N filters cover hydrogen recombination lines. We show these as orange stick spectra (i.e., they have no width), with peak levels set as the ratio of the labeled line emissivity to that of Br $\alpha$  under case B conditions for  $n_e = 10^4 \text{ cm}^{-3}$  and  $T = 10^4 \text{ K}$  (see §4.2). The CO gas absorption optical depth  $\tau$  is shown using a synthetic spectrum with  $N(\text{CO}) = 10^{16}$ ,  $T = 50 \text{ K}$ , and  $\sigma = 5 \text{ km s}^{-1}$  (§4.3). The Pf $\beta$  line lies between the CO v=0-1 J=0-1 and J=1-2 transitions ( $\Delta v \approx 200 - 300 \text{ km s}^{-1}$ ), while H $\epsilon$  is close to the J=1-0 transition ( $\Delta v \approx 100 \text{ km s}^{-1}$ ). These lines would therefore require very large broadening and/or doppler shift to overlap. The red curves show CO and CO<sub>2</sub> ice optical depth  $\tau$  using Hudgins et al. (1993) transmission curves, which overlap with the recombination lines.

using Yurchenko et al. (2018) as an implementation reference.

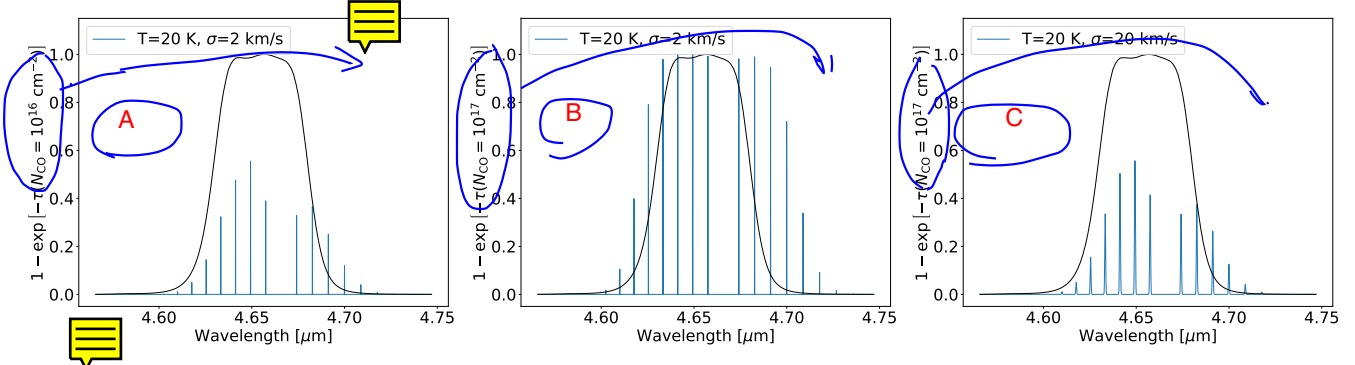
Figure 6 shows example optical depth spectra overlaid on the transmission profile of the F466N filter. The J=1-1 and J=0, 1, 2, 3 to J+1 transitions and the v=0-1 J=1-0 transition all lay within the range that F466N has > 50% of peak transmission. The maximum absorption in this filter occurs for temperatures between 10-20 K, while for gas in the F466N we expect temperatures near 50-100 K (Ginsburg et al. 2016; Immer et al. 2012; Krieger et al. 2017). At higher temperatures, a large fraction of CO molecules are in states that favor produce transitions outside of the F466N band, reducing the absorption. However, it is likely that much of the CO gas is at moderate densities ( $H_2 \lesssim 10^4 \text{ cm}^{-3}$ ) and therefore is sub-thermally excited, which would concentrate the CO molecules into the lower-J levels, balancing out this effect. Nevertheless, the LTE models shown in Figure 6 capture the range of expected behavior.

We model the CO gas absorption for the expected range of line width and column density in the Galactic Center. For narrow line widths, such as those caused by thermal broadening at  $T < 100 \text{ K}$ , the absorption is negligible. In the Galactic center, there is significant doppler broadening that is generally attributed to turbulence. The total linewidth in the cloud may range from  $\sigma \sim 5 - 20 \text{ km/s}$  (Henshaw et al. 2019). CO column densities will span the full range from effectively zero (since CO is destroyed by UV at  $A_V \lesssim 2$

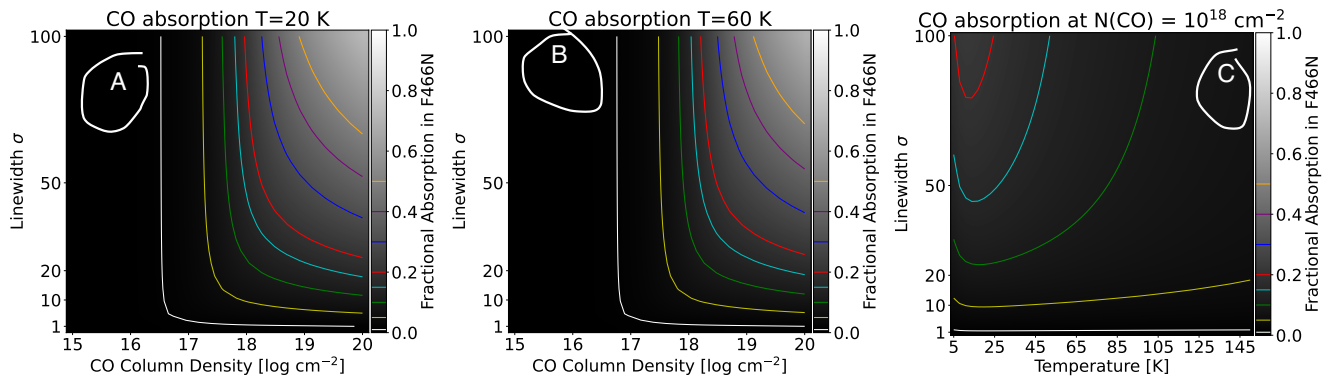
to  $\sim a few \times 10^{19} \text{ cm}^{-2}$  (Rathborne et al. 2015) assuming  $X_{\text{CO}} = 10^{-4}$ . In our observations, we detect stars at  $\lambda = 2 \mu\text{m}$  only at intermediate column densities, most likely below  $A_V < 8$  ( $H_2 < 10^{23} \text{ cm}^{-2}$ ), since dust extinction hides the stellar continuum at higher column density.

Figure 7 summarizes the modeling results. Given the plausible range of column density and line width, the total CO gas absorption in F466N may range from ~ 1% to at most  $\lesssim 20\%$ .

At the column densities where the absorption is easily detectable (fractional absorption  $\gtrsim 0.1$  results in a change in magnitude  $\Delta m \gtrsim 0.1$ ; green line in Figure 7), change in linewidth dominates over the change in column density or temperature. The foreground Galactic disk clouds, which have narrow lines, produce relatively little absorption; we therefore argue that intervening material between the Galactic center is not primarily responsible for blocking the stars. These models also imply that, even at very extreme column densities ( $N_{\text{CO}} > 10^{19} \text{ cm}^{-2}$ ), “normal” galactic disk clouds with  $\sigma < 10 \text{ km s}^{-1}$  will produce minimal CO absorption in the F466N band, while typical galaxy center and galactic bar clouds with  $\sigma \sim 10 - 50 \text{ km s}^{-1}$  will produce readily detectable absorption. However, even for very broad lines ( $\sigma = 50 \text{ km s}^{-1}$ ) at high column ( $N_{\text{CO}} \sim 10^{19.5} \text{ cm}^{-2}$ ) CO gas produces  $\lesssim 1$  magnitude (< 50%) of absorption.



**Figure 6.** Example spectra showing the optical depth of  $^{12}\text{CO}$   $v=0-1$  superposed on the transmission spectrum of the F466N filter for a variety of physical conditions. The black curve in each case shows the transmission function of the F466N filter. The blue curves show the absorbed light fraction  $1 - e^{-\tau}$ . The left shows the effect of this absorption for a low column density case ( $N(\text{CO}) = 1 \times 10^{16} \text{ cm}^{-2}$  or  $N(\text{H}_2) = 1 \times 10^{20} \text{ cm}^{-2}$  for a typical CO abundance of  $X_{\text{CO}} = 10^{-4}$ ). The middle shows  $N(\text{CO}) = 10^{17} \text{ cm}^{-2}$  ( $N(\text{H}_2) = 10^{21} \text{ cm}^{-2}$ ). The right shows transmission for CO column density  $10^{17} \text{ cm}^{-2}$  ( $N(\text{H}_2) = 1 \times 10^{21} \text{ cm}^{-2}$ ) but with a broader line, illustrating that more of the band is absorbed but the peak optical depth is lower.



**Figure 7.** The fractional absorption by gas-phase CO  $v=0-1$  within the F466N band for 20 K (left), 60 K (middle), and at a fixed column density  $N_{\text{CO}} = 10^{18} \text{ cm}^{-2}$  (right). The grayscale shows the fractional absorption as labeled in the colorbar; an absorption  $\leq 1.0$  implies that no photons are received in the band. Colored lines are placed at levels=[0.01, 0.05, 0.1, 0.15, 0.2, 0.3, 0.4, 0.5] with colors=[white, yellow, green, cyan, red, blue, purple, orange], respectively, to help guide the eye. These levels correspond to magnitude differences  $\Delta m = [0.011, 0.056, 0.114, 0.176, 0.242, 0.387, 0.555, 0.753]$ .

430

#### 4.4. CO ice absorption

431 While we show above that CO gas can produce a substantial amount of absorption, the observed absorption depths 432 reach levels difficult to explain with gas alone. Figure 7 433 shows that CO column densities  $N(\text{CO}) > 10^{19.5} \text{ cm}^{-2}$ , 434 implying  $N(\text{H}_2) > 3 \times 10^{23} \text{ cm}^{-2}$ , are required to explain 435 the  $\gtrsim 2$  magnitudes of F466N absorption shown in Figure 4. 436 Such high column densities are rare in The Brick (Rathborne 437 et al. 2014a), occurring primarily in the inner regions (see 438 their Figure 2) and in dense cores (Walker et al. 2021), while 439 the high-extinction and high-CO-absorption stars we detect 440 are primarily in the outskirts (Figure 3). Stars behind these 441 high column density clouds would be too extincted to detect in the 442 shorter wavelength band, the highest extinction we report in 443 Figure 10 is  $A_V \sim 1$ , or  $N(\text{H}_2) \sim 10^{24} \text{ cm}^{-2}$ . Additionally, in 444 Section 4.2, we showed that CO gas is unlikely to absorb re- 445 combination lines. We therefore examine the possibility that 446

447 ice absorption is responsible for the observed F466N defi-  
448 ciencies deficits.

449 There is evidence that The Brick contains some ice, but 450 that CO is not entirely frozen out. Pure CO ice forms at low 451 temperatures,  $T < 20 \text{ K}$  (Hudgins et al. 1993). The aver- 452 age dust temperature in The Brick is close to 20 K (Tang 453 et al. 2021), so it is probable that some of the volume of 454 The Brick is cold enough to freeze CO. The Brick exhibits 455 signs of substantial freezeout in its center based on gas ob- 456 servations (Rathborne et al. 2014b), but still has substantial 457 gas-phase CO detected (Ginsburg et al. 2016; Rigby et al. 458 2016; Eden et al. 2020). It is likely that much of the ob- 459 served gas-phase CO is on the cloud surface, while further 460 into the interior, CO is more completely frozen out.

461

##### 4.4.1. CO Ice modeling

F466N

462 To model CO ice absorption, we convolve the filter trans- 463 mission curve with a synthetic model spectrum. We start with 464 a 4000 K PHOENIX stellar atmosphere (Husser et al. 2013)

stellar

as the base model, then examine the fractional flux lost in the F466N band as a function of CO column density. We retrieve optical constants for pure CO ice and CO mixed with OCS and CH<sub>4</sub> in a 20:1 ratio from Hudgin et al. (1993) via the JPL Optical Constants Database<sup>6</sup>. Figure 8 shows the effects of ice absorption<sup>7</sup>: at N(CO) ≈ 10<sup>19</sup> cm<sup>-2</sup>, we expect ≈ 0.5 – 1 magnitudes of absorption from the ice band. Figure 9 shows similar plots for the F405N and F410M filters and CO<sub>2</sub> ice to demonstrate that CO<sub>2</sub> ice can have some effect, but a lesser one, on our observed colors. The highest observed column density within The Brick, based on ALMA dust emission observations with ∼ 3'' resolution, is N(H<sub>2</sub>) ∼ 5 × 10<sup>23</sup> cm<sup>-2</sup> (Rathborne et al. 2014a), which implies upper limit on the ice column density N(CO) < 5 × 10<sup>18</sup> cm<sup>-2</sup>. We assume the CO/H<sub>2</sub> ratio is 10<sup>-4</sup> and a gas-to-dust mass ratio is 100. That means that, if all of the CO is frozen out into pure CO ice, in the highest column-density line-of-sight, absorption could just about reach 1.2 magnitudes (~ 65%). We also considered the possibility that CO is embedded in other ices (e.g., H<sub>2</sub>O and CH<sub>3</sub>OH; Pontoppidan et al. 2003; Boogert et al. 2008), but found little practical difference from pure CO ice when using the Hudgin et al. (1993) and Rocha et al. (2016) optical constants.

#### 4.4.2. CO ice as a function of extinction

We compare the inferred extinction to the CO ice column to obtain a coarse estimate of how CO ice varies with A<sub>V</sub>. We use [F182M]-[F212N] color to estimate A<sub>V</sub> using the CT06 extinction curve, which we justify by comparing to ground-based GALACTICNUCLEUS colors in Appendix A.

To measure CO absorption, we use the F410M-F466N color. Figure 10c shows that the F410M-F466N color gets bluer at higher extinction. We calculate the absorption from pure CO ice in the F466N band to obtain a mapping from N(CO) to F410M-F466N color. We deredden our measured F410M-F466N color using the A<sub>V</sub> computed above with the CT06 extinction curve. Figure 10 shows the resulting N(CO) as a function of A<sub>V</sub>.

The red curve in Figure 10 shows the maximum possible CO at each A<sub>V</sub> adopting standard values of N(H<sub>2</sub>) = 2.21 × 10<sup>21</sup> A<sub>V</sub> (Güver & Özel 2009) and CO abundance relative to hydrogen X<sub>CO</sub> = 10<sup>-4</sup>. Some of the data points reside above this curve, suggesting that one or both of these assumptions may be incorrect, which we will evaluate further in §5.1. The CO vs A<sub>V</sub> correlation is similar to that in Boogert et al. (2015) extrapolated to much higher column densities.

<sup>6</sup> <https://ssmc.nasa.gov/page/toe>

<sup>7</sup> Figure 8 includes the F470N filter, which we have not used in this work, to caution other JWST users that there may be significant, albeit weaker, CO absorption in this filter.

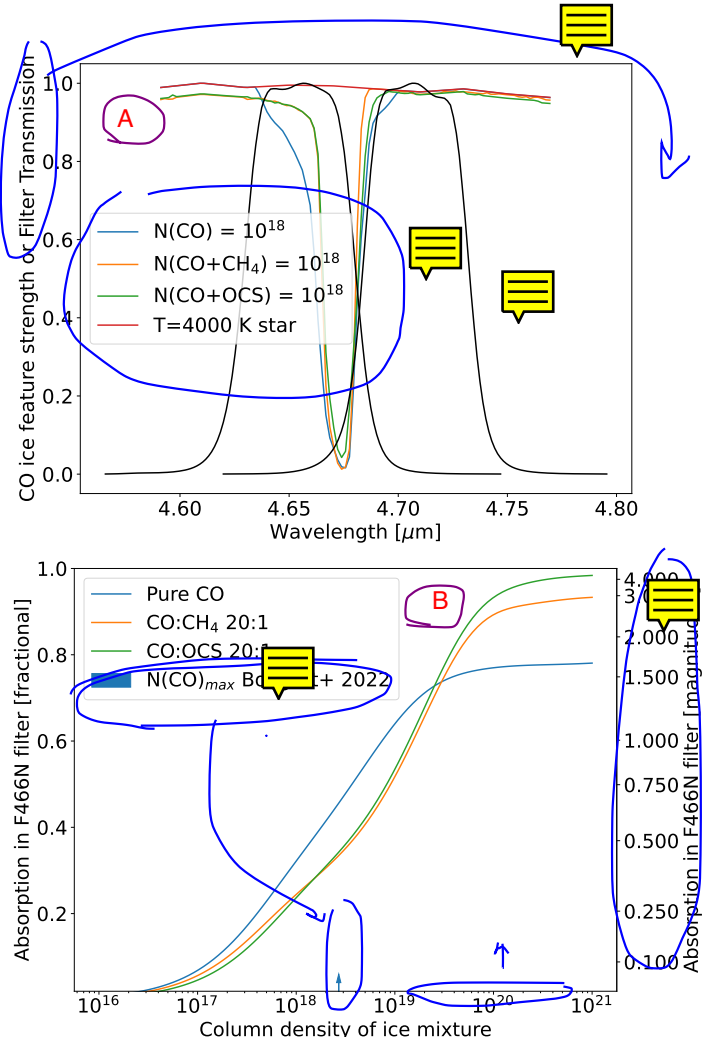


**Figure 8.** (left) Overlap of the transmission profiles of the F466N and F470N filters with CO ice bands. The absorption profiles are produced using Hudgin et al. (1993) opacity measurements. (right) B: The expected absorption as a function of column density in the F466N band for three different CO ices. The absorption is given in fractional value on the left and magnitudes on the right. The arrow shows the highest observed column density of CO ice from the Boogert et al. (2022) sample of high-mass young stellar objects to indicate the range of physically plausible values.

While there is a good overall correlation between N(CO) and A<sub>V</sub>, the dispersion at any given A<sub>V</sub> is large, of order of magnitude. Such a large scatter indicates a wide range of conditions, with many lines-of-sight containing little CO at the lowest observed A<sub>V</sub>.

## 5. DISCUSSION

### 5.1. CO produces F466N absorption

The CO ice model qualitatively explain most of the observed F466N blueing. However, neither the gas nor ice models appear to quantitatively explain the most deeply absorbed sources. In both the gas and ice absorption cases, it is possible to achieve substantial absorption in the F466N band,

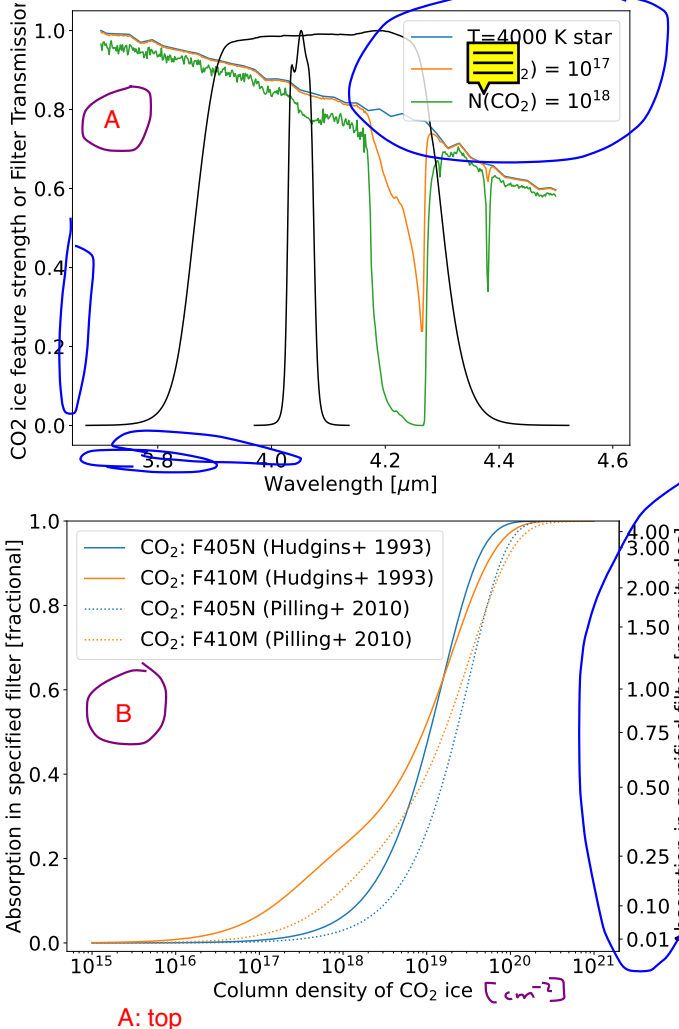


**Figure 9.** (left) Overlap of the transmission profiles of the F405N and F410M filters with CO<sub>2</sub> ice absorption models superimposed on a PHOENIX 4000 K stellar photosphere model. The absorption constants are for pure CO<sub>2</sub> ice from Hudgins et al. (1993) via the Optical Constants Database (OCDB). (right) Bottom: expected absorption as a function of column density in the F405N and F410M bands. The absorption is given in fractional value on the left and magnitudes on the right.

enough to be easily detected, but less than the 1-2 magnitudes seen in Figure 4 if typical CO abundance and gas-to-dust ratios are used.

One possible explanation lies in our assumptions about how to convert column densities between dust, molecular hydrogen, and CO: if the CO/H<sub>2</sub> ratio is greater than the assumed 10<sup>-4</sup>, or the gas-to-dust ratio is lower than 100 (e.g. Giannetti et al. 2017), the total CO column could be higher. Increasing the CO abundance or decreasing the gas-to-dust ratio would both have the effect of shifting the red dashed line upward in Figure 10. These changes would therefore increase the maximum allowed CO abundance and explain the large observed F466N absorption.

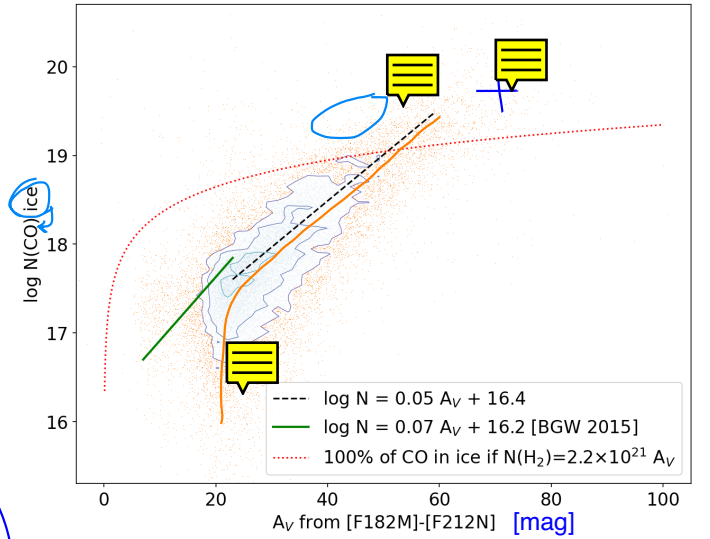


**Figure 10.** N(CO) vs  $A_V$ . The black dashed line is shown as a representative typical value; it is not a fit to the data. The green line is from Boogert et al. (2015, figure 7). The red line shows the CO column density obtained by converting  $N(\text{CO}) = N(\text{H}_2)/10^4$ .  $A_V$  is computed from [F182M]-[F212N] color. We caution that there is likely a systematic calibration issue in several of the filters that affects the absolute  $A_V$ ; the data may shift significantly to either side.

## 5.2. Ice freezeout and gas thermodynamics

The presence of significant quantities of CO ice in The Brick highlights the fact that the dust is significantly colder than the gas. Gas temperatures in the CMZ generally (Ginsburg et al. 2016; Krieger et al. 2017), and The Brick specifically (Johnston et al. 2014), are observed to be high,  $T \gtrsim 50$  K, and in many locations  $T > 100$  K. Freezing of pure CO into ice is expected to occur at dust temperatures  $T \lesssim 20$  K, though CO can be integrated into H<sub>2</sub>O and CH<sub>3</sub>OH ices that freeze out at higher temperatures ( $T \gtrsim 80$  K; Boogert et al. 2015; Garrod & Herbst 2006). The dust temperatures observed in The Brick have been in the range  $T \sim 20 - 30$  K, albeit at lower resolution (Marsh et al. 2016; Tang et al. 2021), which is somewhat too warm for pure CO freezeout but cold enough to freeze other molecules. However, dust temperature measurements are biased toward former dust, since it is brighter, so it is likely that colder dust is present deep inside The Brick.

Both an excess of CO in Galactic Center gas, and freeze-out during gravitational collapse, may result in a change in the effective equation of state of the gas. In the dense molecular medium ( $n \gtrsim 10^3$  cm<sup>-3</sup>) that comprises The Brick, CO is the dominant gas-phase coolant (Ginsburg et al. 2016). If the CO abundance is greater than in the solar neighborhood (§5.1), we expect more efficient cooling in the lower-density outskirts of CMZ clouds. By contrast, as the clouds collapse to higher density, there may be a point at which the CO has frozen out to the point that it is no longer the domi-

563 nant cool~~ing~~ but where the densities are still too low for dust  
 564 to be efficient. We suggest that variations in the cooling function  
 565 should be explored in future simulations of CMZ cloud  
 566 thermodynamics like those in Clark et al. (2013).

### 567 5.3. Broader Implications & Future Applications

568 The prevalence of CO ice in our own Galactic Center hints  
 569 that ice is likely widespread in galactic centers generally. At  
 570 least in the local universe, ~~JWST~~ observations using the long-  
 571 wavelength narrowband filters should carefully treat CO ab-  
 572 sorption in addition to extinction effects. Our Figure 10 gives  
 573 a first empirical tool to link extinction and ice, though we  
 574 caution that the large scatter demonstrated in that plot limits  
 575 the usefulness of the linear relation given in its legend.

576 The easy detection of ices in ~~this~~ the F466N filter also  
 577 opens opportunities to better understand dust and ice in the  
 578 ISM and to understand cloud structures. While NIRSpec will  
 579 have the capability of studying hundreds of stars with ice ab-  
 580 sorption in detail, NIRCam observations can easily measure  
 581 tens of thousands of sightlines simultaneously, enabling de-  
 582tailed correlation analyses like those shown in Fig. 10. By  
 583 adding comparable-resolution gas observations from ALMA,  
 584 it should be possible to trace the freezeout of CO from gas to  
 585 ice in detail. With a few other bands, such as F300M and  
 586 F335M, it will be possible to track H<sub>2</sub>O and CH<sub>3</sub>OH ice and  
 587 determine when and how much CO is incorporated into H<sub>2</sub>O  
 588 ice, which freezes at a substantially higher temperature.

589 The overlap of the CO ice feature with Pfβ+Hue also opens  
 590 the possi~~bility~~ of making ∼0.1'' resolution maps of CO ice  
 591 absorption. From the Paα/Bra ratio, we can determine the  
 592 dust extinction on a per-pixel basis, which will enable spe-  
 593 cific measurement of CO ice absorption ~~from the Bra/Pfβ~~  
 594 ~~ratio~~. Since the CO ice feature affects the Pfβ line, but CO  
 595 gas does not, this approach will also allow us to distinguish  
 596 whether ice or gas is the dominant absorber on most sight-  
 597 lines.

598

## 6. CONCLUSIONS

599 We report observations of G0.253+0.015, an infrared dark  
 600 cloud known as “The Brick”, with JWST’s NIRCam in  
 601 narrow-band filters. We produce a crossmatched photometric  
 602 catalog using the `crowdsource` package. We find 377,593  
 603 unique sources, of which 59,266 are detected in all six pho-  
 604 tometric bands.

605 In this first publication on these data, we show that there is  
 606 significant absorption toward stars in the F466N band, which  
 607 is caused by CO ice and gas. We argue that ice is predom-  
 608 inant along most sightlines and provide modeling results to  
 609 show the effect of ice and gas absorption on this and other  
 610 JWST filters. While CO absorption is a suitable explanation  
 611 for the observed F466N absorption, the quantities of both  
 612 ice and gas required to produce the observed absorption is  
 613 in some tension with the observed line-of-sight column den-  
 614 sity. This result indicates that the standard abundance of CO  
 615 ( $X_{CO} = 10^{-4}$ ) and/or the gas-to-dust ratio (100) are too low  
 616 for the Galactic Center environment.

617 *Acknowledgements* We thank Eddie Schlaflfy and Andrew  
 618 Saydjari for their assistance with `crowdsource` technical  
 619 issues. AG acknowledges support from STSCI grant JWST-  
 620 GO-02221.001-A, and from the NSF through AST 2008101,  
 621 AST 220651, and CAREER 2142300. CB gratefully ac-  
 622 knowledges funding from the National Science Foundation  
 623 under Award Nos. 1816715, 2108938, 2206510, and CA-  
 624 REER 2145689, as well as from the National Aeronautics  
 625 and Space Administration through the Astrophysics Data  
 626 Analysis Program under Award No. 21-ADAP21-0179 and  
 627 through the SOFIA archival research program under Award  
 628 No. 09\_0540. XL acknowledges support from the Na-  
 629 tional Natural Science Foundation of China (NSFC) through  
 630 grant No. 12273090, and the Natural Science Foundation  
 631 of Shanghai (No. 23ZR1482100). JDH gratefully acknowl-  
 632 edges financial support from the Royal Society (University  
 633 Research Fellowship; URF\R1\221620)

## REFERENCES

- 634 An, D., Ramírez, S. V., Sellgren, K., et al. 2011, ApJ, 736, 133,  
 635 doi: [10.1088/0004-637X/736/2/133](https://doi.org/10.1088/0004-637X/736/2/133)
- 636 Ao, Y., Henkel, C., Menten, K. M., et al. 2013, A&A, 550, A135,  
 637 doi: [10.1051/0004-6361/201220096](https://doi.org/10.1051/0004-6361/201220096)
- 638 Bally, J., Rathborne, J. M., Longmore, S. N., et al. 2014, ApJ, 795,  
 639 28, doi: [10.1088/0004-637X/795/1/28](https://doi.org/10.1088/0004-637X/795/1/28)
- 640 Boogert, A. C. A., Brewer, K., Brittain, A., & Emerson, K. S.  
 641 2022, ApJ, 941, 32, doi: [10.3847/1538-4357/ac9b4a](https://doi.org/10.3847/1538-4357/ac9b4a)
- 642 Boogert, A. C. A., Gerakines, P. A., & Whittet, D. C. B. 2015,  
 643 ARA&A, 53, 541, doi: [10.1146/annurev-astro-082214-122348](https://doi.org/10.1146/annurev-astro-082214-122348)
- 644 Boogert, A. C. A., Pontoppidan, K. M., Knez, C., et al. 2008, ApJ,  
 645 678, 985, doi: [10.1086/533425](https://doi.org/10.1086/533425)
- 646 Brasseur, C. E., Rogers, T., Donaldson, T., et al. 2020, in  
 647 Astronomical Society of the Pacific Conference Series, Vol. 522,  
 648 Astronomical Data Analysis Software and Systems XXVII, ed.
- 649 P. Ballester, J. Ibsen, M. Solar, & K. Shortridge, 97
- 650 Chiar, J. E., & Tielens, A. G. G. M. 2006, ApJ, 637, 774,  
 651 doi: [10.1086/498406](https://doi.org/10.1086/498406)
- 652 Chiar, J. E., Tielens, A. G. G. M., Whittet, D. C. B., et al. 2000,  
 653 ApJ, 537, 749, doi: [10.1086/309047](https://doi.org/10.1086/309047)
- 654 Churchwell, E., Babler, B. L., Meade, M. R., et al. 2009, PASP,  
 655 121, 213, doi: [10.1086/597811](https://doi.org/10.1086/597811)
- 656 Clark, P. C., Glover, S. C. O., Ragan, S. E., Shetty, R., & Klessen,  
 657 R. S. 2013, ApJL, 768, L34, doi: [10.1088/2041-8205/768/2/L34](https://doi.org/10.1088/2041-8205/768/2/L34)

- 658 Eden, D. J., Moore, T. J. T., Currie, M. J., et al. 2020, MNRAS,  
 659 498, 5936, doi: [10.1093/mnras/staa2734](https://doi.org/10.1093/mnras/staa2734)
- 660 Federrath, C., Rathborne, J. M., Longmore, S. N., et al. 2016, ApJ,  
 661 832, 143, doi: [10.3847/0004-637X/832/2/143](https://doi.org/10.3847/0004-637X/832/2/143)
- 662 Fritz, T. K., Gillessen, S., Dodds-Eden, K., et al. 2011, ApJ, 737,  
 663 73, doi: [10.1088/0004-637X/737/2/73](https://doi.org/10.1088/0004-637X/737/2/73)
- 664 Garrod, R. T., & Herbst, E. 2006, A&A, 457, 927,  
 665 doi: [10.1051/0004-6361:20065560](https://doi.org/10.1051/0004-6361:20065560)
- 666 Giannetti, A., Leurini, S., König, C., et al. 2017, A&A, 606, L12,  
 667 doi: [10.1051/0004-6361/201731728](https://doi.org/10.1051/0004-6361/201731728)
- 668 Ginsburg, A., Sokolov, V., de Val-Borro, M., et al. 2022, AJ, 163,  
 669 291, doi: [10.3847/1538-3881/ac695a](https://doi.org/10.3847/1538-3881/ac695a)
- 670 Ginsburg, A., Henkel, C., Ao, Y., et al. 2016, A&A, 586, A50,  
 671 doi: [10.1051/0004-6361/201526100](https://doi.org/10.1051/0004-6361/201526100)
- 672 Ginsburg, A., Sipőcz, B. M., Brasseur, C. E., et al. 2019, AJ, 157,  
 673 98, doi: [10.3847/1538-3881/aafc33](https://doi.org/10.3847/1538-3881/aafc33)
- 674 Gordon, K. D., Misselt, K. A., Bouwman, J., et al. 2021, ApJ, 916,  
 675 33, doi: [10.3847/1538-4357/ac00b7](https://doi.org/10.3847/1538-4357/ac00b7)
- 676 Güver, T., & Özel, F. 2009, MNRAS, 400, 2050,  
 677 doi: [10.1111/j.1365-2966.2009.15598.x](https://doi.org/10.1111/j.1365-2966.2009.15598.x)
- 678 Henshaw, J. D., Longmore, S. N., & Kruijssen, J. M. D. 2016,  
 679 MNRAS, 463, L122, doi: [10.1093/mnrasl/slw168](https://doi.org/10.1093/mnrasl/slw168)
- 680 Henshaw, J. D., Ginsburg, A., Haworth, T. J., et al. 2019, MNRAS,  
 681 485, 2457, doi: [10.1093/mnras/stz471](https://doi.org/10.1093/mnras/stz471)
- 682 Henshaw, J. D., Kruijssen, J. M. D., Longmore, S. N., et al. 2020,  
 683 Nature Astronomy, 4, 1064, doi: [10.1038/s41550-020-1126-z](https://doi.org/10.1038/s41550-020-1126-z)
- 684 Henshaw, J. D., Krumholz, M. R., Butterfield, N. O., et al. 2022,  
 685 MNRAS, 509, 4758, doi: [10.1093/mnras/stab3039](https://doi.org/10.1093/mnras/stab3039)
- 686 Hudgins, D. M., Sandford, S. A., Allamandola, L. J., & Tielens,  
 687 A. G. G. M. 1993, ApJS, 86, 713, doi: [10.1086/191796](https://doi.org/10.1086/191796)
- 688 Husser, T. O., Wende-von Berg, S., Dreizler, S., et al. 2013, A&A,  
 689 553, A6, doi: [10.1051/0004-6361/201219058](https://doi.org/10.1051/0004-6361/201219058)
- 690 Immer, K., Menten, K. M., Schuller, F., & Lis, D. C. 2012, A&A,  
 691 548, A120, doi: [10.1051/0004-6361/201219182](https://doi.org/10.1051/0004-6361/201219182)
- 692 Jang, D., An, D., Sellgren, K., et al. 2022, ApJ, 930, 16,  
 693 doi: [10.3847/1538-4357/ac5d51](https://doi.org/10.3847/1538-4357/ac5d51)
- 694 Johnston, K. G., Beuther, H., Linz, H., et al. 2014, A&A, 568,  
 695 A56, doi: [10.1051/0004-6361/201423943](https://doi.org/10.1051/0004-6361/201423943)
- 696 Jones, P. A., Burton, M. G., Cunningham, M. R., et al. 2012,  
 697 MNRAS, 419, 2961, doi: [10.1111/j.1365-2966.2011.19941.x](https://doi.org/10.1111/j.1365-2966.2011.19941.x)
- 698 Kauffmann, J., Pillai, T., & Zhang, Q. 2013, ApJL, 765, L35,  
 699 doi: [10.1088/2041-8205/765/2/L35](https://doi.org/10.1088/2041-8205/765/2/L35)
- 700 Krieger, N., Ott, J., Beuther, H., et al. 2017, ApJ, 850, 77,  
 701 doi: [10.3847/1538-4357/aa951c](https://doi.org/10.3847/1538-4357/aa951c)
- 702 Kruijssen, J. M. D., Dale, J. E., & Longmore, S. N. 2015, MNRAS,  
 703 447, 1059, doi: [10.1093/mnras/stu2526](https://doi.org/10.1093/mnras/stu2526)
- 704 Launhardt, R., Zylka, R., & Mezger, P. G. 2002, A&A, 384, 112,  
 705 doi: [10.1051/0004-6361:20020017](https://doi.org/10.1051/0004-6361:20020017)
- 706 Li, G., Gordon, I. E., Rothman, L. S., et al. 2015, ApJS, 216, 15,  
 707 doi: [10.1088/0067-0049/216/1/15](https://doi.org/10.1088/0067-0049/216/1/15)
- 708 Lis, D. C., & Carlstrom, J. E. 1994, ApJ, 424, 189,  
 709 doi: [10.1086/173882](https://doi.org/10.1086/173882)
- 710 Lis, D. C., Carlstrom, J. E., & Keene, J. 1991, ApJ, 380, 429,  
 711 doi: [10.1086/170601](https://doi.org/10.1086/170601)
- 712 Lis, D. C., & Menten, K. M. 1998, ApJ, 507, 794,  
 713 doi: [10.1086/306366](https://doi.org/10.1086/306366)
- 714 Lis, D. C., Menten, K. M., Serabyn, E., & Zylka, R. 1994, ApJL,  
 715 423, L39, doi: [10.1086/187230](https://doi.org/10.1086/187230)
- 716 Lis, D. C., Serabyn, E., Zylka, R., & Li, Y. 2001, ApJ, 550, 761,  
 717 doi: [10.1086/319815](https://doi.org/10.1086/319815)
- 718 Longmore, S. N., Rathborne, J., Bastian, N., et al. 2012, ApJ, 746,  
 719 117, doi: [10.1088/0004-637X/746/2/117](https://doi.org/10.1088/0004-637X/746/2/117)
- 720 Lutz, D., Feuchtgruber, H., Genzel, R., et al. 1996, A&A, 315,  
 721 L269
- 722 Marsh, K. A., Ragan, S. E., Whitworth, A. P., & Clark, P. C. 2016,  
 723 MNRAS, 461, L16, doi: [10.1093/mnrasl/slw080](https://doi.org/10.1093/mnrasl/slw080)
- 724 Mills, E. A. C., Butterfield, N., Ludovici, D. A., et al. 2015, ApJ,  
 725 805, 72, doi: [10.1088/0004-637X/805/1/72](https://doi.org/10.1088/0004-637X/805/1/72)
- 726 Mills, E. A. C., Ginsburg, A., Immer, K., et al. 2018, ApJ, 868, 7,  
 727 doi: [10.3847/1538-4357/aae581](https://doi.org/10.3847/1538-4357/aae581)
- 728 Moneti, A., Cernicharo, J., & Pardo, J. R. 2001, ApJL, 549, L203,  
 729 doi: [10.1086/319168](https://doi.org/10.1086/319168)
- 730 Moultaka, J., Eckart, A., & Schödel, R. 2009, ApJ, 703, 1635,  
 731 doi: [10.1088/0004-637X/703/2/1635](https://doi.org/10.1088/0004-637X/703/2/1635)
- 732 Nogueras-Lara, F., Schödel, R., Neumayer, N., & Schultheis, M.  
 733 2021, A&A, 647, L6, doi: [10.1051/0004-6361/202140554](https://doi.org/10.1051/0004-6361/202140554)
- 734 Nogueras-Lara, F., Schödel, R., Gallego-Calvente, A. T., et al.  
 735 2019, A&A, 631, A20, doi: [10.1051/0004-6361/201936263](https://doi.org/10.1051/0004-6361/201936263)
- 736 Petkova, M. A., Kruijssen, J. M. D., Kluge, A. L., et al. 2023,  
 737 MNRAS, 520, 2245, doi: [10.1093/mnras/stad229](https://doi.org/10.1093/mnras/stad229)
- 738 Pillai, T., Kauffmann, J., Tan, J. C., et al. 2015, ApJ, 799, 74,  
 739 doi: [10.1088/0004-637X/799/1/74](https://doi.org/10.1088/0004-637X/799/1/74)
- 740 Pontoppidan, K. M., Fraser, H. J., Dartois, E., et al. 2003, A&A,  
 741 408, 981, doi: [10.1051/0004-6361:20031030](https://doi.org/10.1051/0004-6361:20031030)
- 742 Rathborne, J. M., Longmore, S. N., Jackson, J. M., et al. 2014a,  
 743 ApJL, 795, L25, doi: [10.1088/2041-8205/795/2/L25](https://doi.org/10.1088/2041-8205/795/2/L25)
- 744 —. 2014b, ApJ, 786, 140, doi: [10.1088/0004-637X/786/2/140](https://doi.org/10.1088/0004-637X/786/2/140)
- 745 —. 2015, ApJ, 802, 125, doi: [10.1088/0004-637X/802/2/125](https://doi.org/10.1088/0004-637X/802/2/125)
- 746 Rigby, A. J., Moore, T. J. T., Plume, R., et al. 2016, MNRAS, 456,  
 747 2885, doi: [10.1093/mnras/stv2808](https://doi.org/10.1093/mnras/stv2808)
- 748 Rocha, W. R. M., Pilling, S., de Barros, A. L. F., et al. 2016, arXiv  
 749 e-prints, arXiv:1609.04684, doi: [10.48550/arXiv.1609.04684](https://doi.org/10.48550/arXiv.1609.04684)
- 750 Rodríguez, L. F., & Zapata, L. A. 2013, ApJL, 767, L13,  
 751 doi: [10.1088/2041-8205/767/1/L13](https://doi.org/10.1088/2041-8205/767/1/L13)
- 752 Saito, R. K., Hempel, M., Minniti, D., et al. 2012, A&A, 537,  
 753 A107, doi: [10.1051/0004-6361/201118407](https://doi.org/10.1051/0004-6361/201118407)
- 754 Schlafly, E. F. 2021, crowdfuse: Crowded field photometry  
 755 pipeline, Astrophysics Source Code Library, record  
 756 ascl:2106.004. <http://ascl.net/2106.004>

- 757 Storey, P. J., & Hummer, D. G. 1995, MNRAS, 272, 41,  
758 doi: [10.1093/mnras/272.1.41](https://doi.org/10.1093/mnras/272.1.41)
- 759 Tang, Y., Wang, Q. D., & Wilson, G. W. 2021, MNRAS, 505,  
760 2377, doi: [10.1093/mnras/staa3230](https://doi.org/10.1093/mnras/staa3230)
- 761 Tennyson, J., Yurchenko, S. N., Al-Refaie, A. F., et al. 2016,  
762 Journal of Molecular Spectroscopy, 327, 73,  
763 doi: [10.1016/j.jms.2016.05.002](https://doi.org/10.1016/j.jms.2016.05.002)
- 764 Walker, D. L., Longmore, S. N., Bastian, N., et al. 2016, MNRAS,  
765 457, 4536, doi: [10.1093/mnras/stw313](https://doi.org/10.1093/mnras/stw313)
- 766 Walker, D. L., Longmore, S. N., Bally, J., et al. 2021, MNRAS,  
767 503, 77, doi: [10.1093/mnras/stab415](https://doi.org/10.1093/mnras/stab415)
- 768 Yurchenko, S. N., Al-Refaie, A. F., & Tennyson, J. 2018, A&A,  
769 614, A131, doi: [10.1051/0004-6361/201732531](https://doi.org/10.1051/0004-6361/201732531)

770

## APPENDIX

771

## A. COMPARISON TO GALACTICNUCLEUS

772  GALACTICNUCLEUS (GN) survey (Nogueras-Lara et al. 2019, 2021) partially overlaps with the targeted field of view.  
 773 The survey has higher resolution than VVV and therefore presents a better match to our data set, but we chose to use VVV as  
 774 our primary astrometric reference in Section 3 because GN covers only about half of the southern field we observed. GN's higher  
 775 resolution and sensitivity, however, mean that it is more appropriate for photometric comparison.  
 The greater resolution and sensitivity of the GN survey

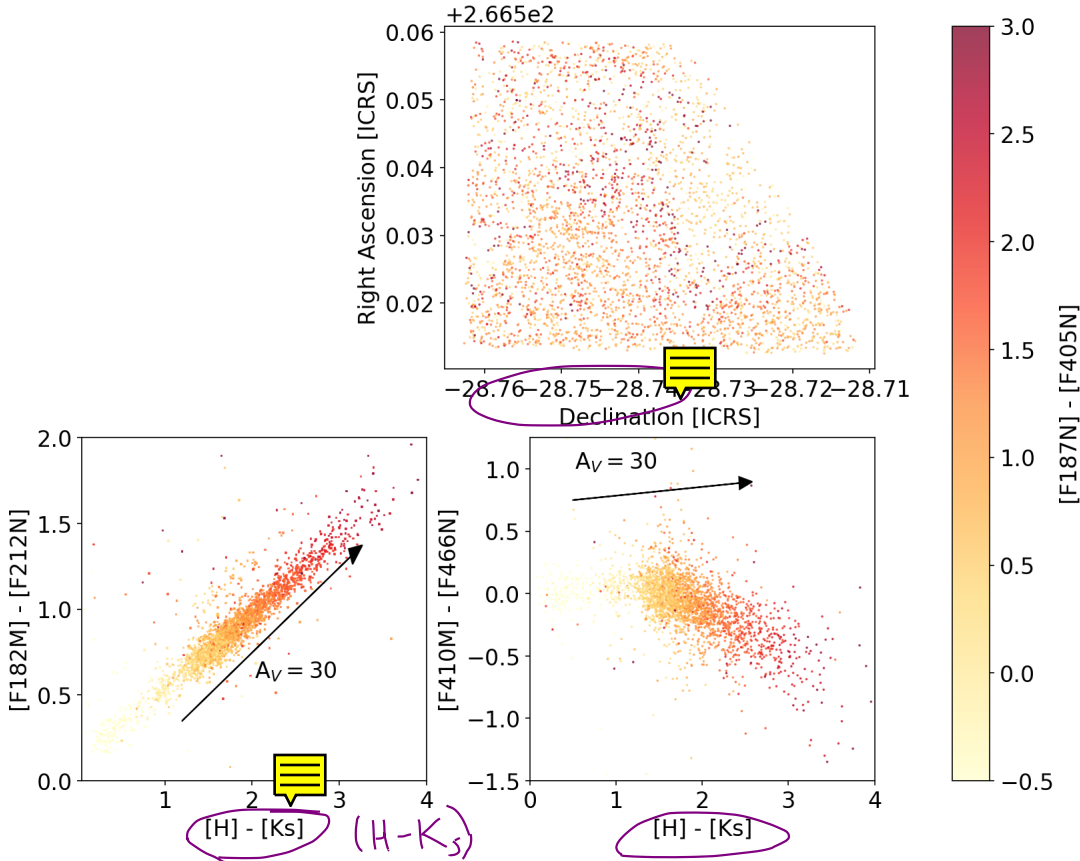


**Figure 11.** Spatial plot (top) and color-color diagrams (bottom) for the subset of our sample cross-matched with the GALACTICNUCLEUS survey (Nogueras-Lara et al. 2021). The left CCD shows our  $[F182M]$ - $[F212N]$  color against the GN  $(H-K_s)$  color, demonstrating that there is very good correlation between these colors and justifying the use of  $[F182M]$ - $[F212N]$  as an extinction estimator. The right CCD shows our  $[F410M]$ - $[F466N]$  against GN  $(H-K_s)$  color, demonstrating that the  $F466N$  bluing is anticorrelated with  $(H-K_s)$  color.

776 To verify our use of narrow- and medium-band filters extinction measurement, we cross-matched our catalog to the GN catalog  
 777 and produce color-color diagrams using GN  $(H-K_s)$  color as a more typical tracer of extinction. We found the closest match  
 778 in our catalog to each GN source and kept all sources with a separation of  $< 0.2''$ . In the field in which GN overlaps our  
 779 observations, there are a total of 16,021 GN sources and 69,918 sources detected in all three of our short-wavelength bands. Of  
 780 the GN sources, 14,557 sources have JWST sources within 0.2 arcseconds, of which 6,844 pass quality criteria specified in §3.4  
 781 for all JWST short-wavelength filters and 3,958 pass quality criteria for all six filters. Figure 11 shows that we reproduce the  
 782 same qualitative result as shown in Figure 4 with these data. This plot demonstrates that our color used to measure extinction in  
 783 the JWST data,  $[F182M]$ - $[F212N]$  color, is well-correlated with the standard ground-based  $(H-K_s)$  color.

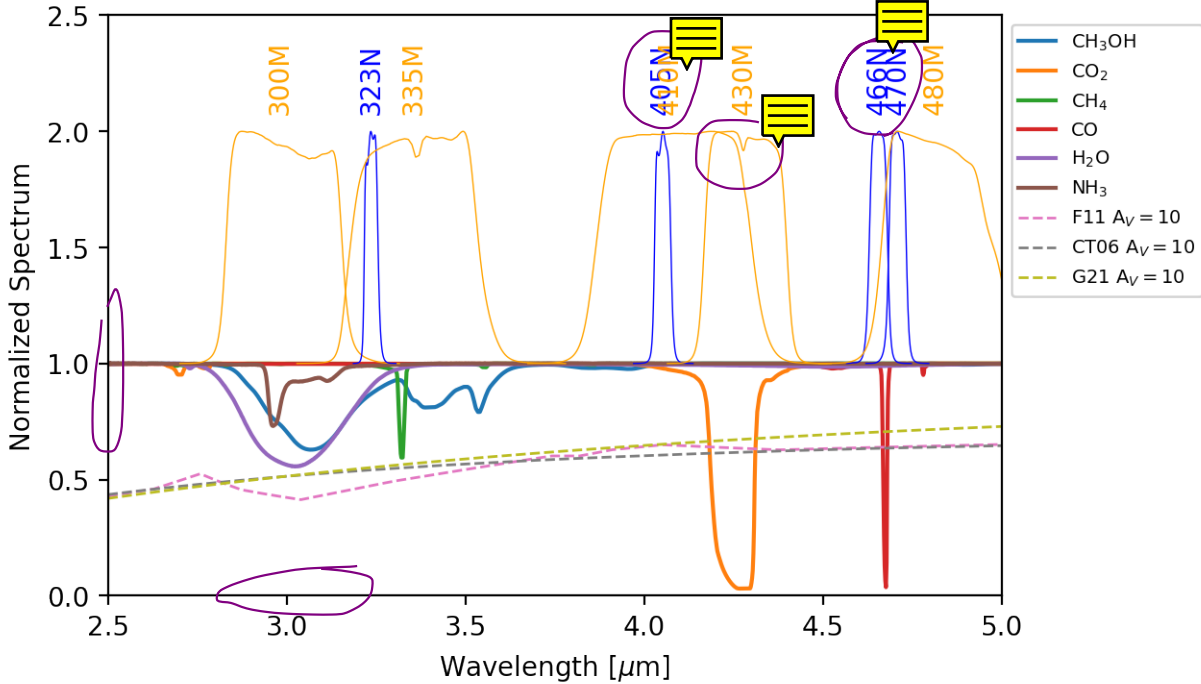


**Figure 12.** Plot of ice absorption and JWST NIRCam filter profiles. The normalized filter profiles are shown as the positive features above 1.0. Orange colors are medium-band, blue are narrow-band. The F405N and F410M filter labels overlap. The ice absorption profiles from several ices are shown in the bottom part of the plot; each ice is plotted with a column density  $N(\text{ice}) = 10^{18} \text{ cm}^{-2}$ . For many of these molecules, this is an unrealistically high column density, but it is helpful to illustrate where absorption occurs. The dashed curves show extinction profiles for three different models: Chiar & Tielens (2006), Fritz et al. (2011), and Gordon et al. (2021).

784

## B. ICE-AFFECTED FILTERS

785 We demonstrate in this paper that ice absorption affects at least the F466N filter in Galactic center photometry. We highlight  
 786 the narrow- and medium-band NIRCam filters that are potentially affected by ices in Figure 12. This plot was made using optical  
 787 constants from the JPL Optical Constants Database<sup>8</sup> using the `icemodels` package<sup>9</sup>.

Is there a “take-away” message the reader should note?

<sup>8</sup> <https://ocdb.smce.nasa.gov/page/toc>

<sup>9</sup> <https://github.com/keflavich/icemodels/>